

Optical and Structural properties of **In-rich** $\text{In}_x\text{Ga}_{1-x}\text{As}$ epitaxial layers on (100) InP for SWIR detectors.

Badreddine Smiri^{1*}, Marwa Ben Arbia¹, Demir Ilkay², Faouzi Saidi^{1,3}, Zied Othmen⁴, Brahim Dkhil⁴, Altuntas Ismail², Elagoz Sezai², Fredj Hassen¹, Hassen Maaref¹.

¹Laboratoire de Micro-optoélectronique et Nanostructures (LR99ES29), Université de Monastir, Faculté des Sciences Monastir, Avenue de l'Environnement 5019 Monastir, Tunisia.

²Department of Nanotechnology Engineering and Nanophotonics Research and Application Center, Cumhuriyet University, 58140 Sivas, Turkey.

³Institut Supérieur des Sciences Appliqués et Technologie de Sousse. Université de Sousse.

⁴Laboratoire Structures, Propriétés et Modélisation des Solides, CentraleSupélec, CNRS-UMR8580, Université Paris-Saclay, 91190 Gif-sur-Yvette, France.

*Corresponding authors: badreddinesmiri@gmail.com

Abstract

In-rich $\text{In}_x\text{Ga}_{1-x}\text{As}$ epitaxial layers were grown on InP (100) substrates by a metalorganic vapor phase epitaxy (MOVPE) technique. The effect of Indium (In) composition on the crystalline quality and optical properties are investigated. High resolution X-ray diffraction (HR-XRD) measurement and Raman scattering spectrum are used to evaluate the crystalline quality, the residual strain and dislocation density property. The number of dislocations in the epitaxial layers is found to increase by increasing the Indium content in order to release the stresses due to the epitaxial clamping. Photoluminescence (PL) measurement is used to characterize the optical properties. At 10 K, PL measurements show that the InGaAs band gap redshifts with the indium content. Moreover, the asymmetry at the low-energy side of the PL peak has been attributed to the presence of localized excitons. In all samples, a blue shift of PL peaks is evidenced by increasing the excitation power density, which is in line with the presence of carrier's localization and non-idealities in this system. Moreover, the temperature-dependence of the PL peak energy displays an unusual red-blue-red shift (S-shaped) behavior when raising the temperature. These observations can be related to the inhomogeneous distribution of indium which gives rise to the appearance of dislocations and other defects which serve as traps for charge carriers. Interestingly, those highly In-content $\text{In}_x\text{Ga}_{1-x}\text{As}$ epitaxial layers show PL emission located between 1637 and 1811 nm (depending on In content) and thus might be suitable for in the design of novel heterostructure devices such as short wave infrared (SWIR) detectors.

Keywords: Rich Indium content, dislocation, lattice mismatch, residual stress, HR-XRD, Raman, PL, Carrier localization,

1. Introduction

InGaAs is one of the most important III-V semiconductor materials attracting attention for their applications in remote sensing, environmental monitoring, optical fiber communication etc [1-6]. Indeed, their bandgap can be engineered in a large range of the infrared spectrum 0.9-3 μm [7] corresponding to the atmospheric transmission window of interest for military, agricultural, scientific and spectroscopic applications [8, 9]. For instance, $\text{In}_x\text{Ga}_{1-x}\text{As}$ ($x=0.53$) grown on InP substrate are commercially available and mature photodetectors with cut-off wavelength at 1.7 μm [9]. As a competitor, II-VI HgCdTe-based materials cover the same wavelength range as InGaAs and many commercial devices exist in the market. However, those HgCdTe detectors require efficient cooling while InGaAs detectors do not need any cooling systems since they can already operate efficiently at room temperature [10]. Moreover, the usually used CdZnTe substrates that have near lattice mismatch with HgCdTe have severe drawbacks such as a lack of large area, a high production cost and, more importantly, a difference in thermal expansion coefficient between those substrates and the silicon readout integrated circuit [11]. Actually, the epitaxial growth and especially the heteroepitaxy of semiconductor materials requires suitable substrate materials which are restricted by lattice mismatch limits. Indeed, the presence of dislocations which appear to relax strains in the active heteroepitaxial layer during the growth can be detrimental to optical and electrical device performances [12].

In case of InGaAs, applications in longer wavelength region ($>1.7\mu\text{m}$) require to increase the indium content, which in counterpart increases the lattice mismatch between rich indium content InGaAs and InP substrate. For example, the 2.5 μm cut-off wavelength photodetectors $\text{In}_{0.83}\text{Ga}_{0.17}\text{As}$ have a lattice mismatch of about + 2.1 % with respect to InP [13]. As a result, many studies have been conducted to improve crystalline and optical quality and surface roughness as well as decrease deep-level defects of highly indium-doped $\text{In}_x\text{Ga}_{1-x}\text{As}$ epitaxial layers. In this context, Xiaoli et al. [14] showed that the high dark current is still one of the critical technology issues for extended wavelength InGaAs detectors. The cut-off wavelength ranges from 1.7 μm to 2.4 μm with the rise of Indium composition from 0.53 to 0.78, but concomitantly the dark current increases about four orders of magnitude. The origin of the enhanced dark current is known to be related to lattice-mismatch between the epitaxial layer and the substrate [14]. For $\text{In}_x\text{Ga}_{1-x}\text{As}$ thin films grown on InP, Liang Zhao et al. [15] used

transmission electron microscopy to show that the observed surface undulation which is enhanced with the increase of mismatch degree is caused by the accumulation of dislocations. Moreover, the high density of such structural defects (cluster effect) in the InGaAs layer, can generate localized trap states near the band edge [16]. Any localization of carriers in InGaAs structures due to lattice disorder, impurities, composition or layer thickness variation... [17-19] has an important effect on their dynamics and thus the properties of the material. A better understanding of the consequences of In content in rich concentration x in $\text{In}_x\text{Ga}_{1-x}\text{As}$ alloy is therefore crucial prior to its integration into opto-electronic applications. This is the aim of the current paper. The crystalline quality, the residual strain, dislocation density and optical responses of In-rich $\text{In}_x\text{Ga}_{1-x}\text{As}$ epitaxial layers are studied here in detail by high-resolution X-ray diffraction (HR-XRD), Raman spectroscopy, power-dependent photoluminescence (PDPL) and temperature-dependent photoluminescence (TDPL) measurements.

2. Experimental details

The $\text{In}_x\text{Ga}_{1-x}\text{As}$ epitaxial layers of thickness 190 nm with different In contents (sample S1: $x = 0.65$, sample S2: $x=0.661$ and sample S3: $x=0.667$) were grown on (100) InP substrate by Metalorganic Vapor Phase Epitaxy (MOVPE) at 560°C . The growth rate is about 3 \AA per second. High purity hydrogen (H_2) and nitrogen (N_2) gases are used as the carrier gas in MOVPE system during the growth. Metal organic (MO) TMGa (Trimethylgallium), TMIIn (Trimethylindium) and hydride AsH_3 (arsine) are used as Ga, In and As precursors, respectively. Gas flow rotation is used to obtain uniform (thickness, composition etc.) epitaxial layers. The hydride and metal-organic sources are introduced as vapor phase into a hot ($\sim 650^\circ\text{C}$) reaction chamber and thermally decomposed (pyrolysis) at growth temperature on the hot substrate located on top of susceptor to form the desired film in the reaction chamber. Then, the samples were characterized by HR-XRD and PL. The HR-XRD measurements were performed using Rigaku SmartLab diffractometer, equipped with a rotating Cu anode (wavelength $K_\alpha=1.54056 \text{ \AA}$) which provides 9kW X-ray power and four bounced Ge (220) monochromator allowing a 2θ precision of 0.0004° . The Raman spectra were acquired using a Horiba T64000 spectrometer at room temperature in a backscattering geometry using the 532 nm-excitation line of an argon-ion laser operating at 10 mW focused to a spot of $50 \mu\text{m}$ in diameter. The scattered light was dispersed using a triple monochromator and the spectra were recorded using a liquid nitrogen cooled CCD. For PL measurements, the samples were mounted in a closed-cycle cryostat with temperature varying from 10 to 300 K, and excited by a 514-nm continuous Ar⁺ laser and a fixed power excitation

of 80 W/cm². Spectral response of the luminescence measurements was dispersed using JOBIN YVON HRD1 monochromator and detected by a cooled InGaAs photodetector.

3. Results and discussions

3. 1. Structural characterizations

The HR-XRD spectrum of the three In_xGa_{1-x}As/InP samples versus 2θ is presented in Figure 1. We have chosen the interval between 61° and 64° where the {004} Bragg peak is located. In this figure, it is clear that the high-intense sharp peaks were derived from InP substrates and the other peaks from In_xGa_{1-x}As layers. According to the HR-XRD data, In_xGa_{1-x}As peaks are on the left side of InP peak for all samples, which means that the film is under compressive strain resulting in an enhancement of the out-of-plane lattice parameter. From HR-XRD measurement of the (004) plane spacing, we it is possible to determine the strain between the In_xGa_{1-x}As epitaxial layers and the substrate as [1]:

$$\frac{\Delta a}{a} = - \frac{\Delta \theta}{\tan(\theta_B)} \quad (1)$$

where Δθ is the measured angular spacing between the epitaxial layer and substrate diffraction peaks and θ_B is the Bragg angle for the InP substrate.

In the Figure. 1, one can also see the possibility to grow relatively rich indium content of In_xGa_{1-x}As (x=0.667) without using any compensation buffer layer. As can be clearly seen, the more the In content is and the stronger the compressive strain is as the Bragg peak is more shifted towards the left side (low 2theta) angles. Moreover, when the mismatch between the InGaAs films and the InP substrate is large, the full width at half maximum (FWHM) of the Bragg peak is bigger while the film thickness keeps constant, meaning that defects, and most likely dislocations, form in order to release the imposed misfit strain by the substrate. Based on the literature, it is possible to evaluate the dislocation density (N_{dis}) in such epitaxial layers according to the following formula [20, 21]:

$$N_{dis} = 2 \frac{(FWHM)^2}{9a_0^2} \quad (2)$$

Where a₀ is the lattice constant of the epitaxial layer. We then determined the dislocation density of the all samples (Table 1). From Table 1, we can see that, increasing the Indium content through x = 0.65, 0.661 and 0.667 leads to an increase in the dislocation density N_{dis} = 2.17, 2.64, and 3.14 (10⁹ cm⁻²), respectively. Yet, the smallest FWHM of 0.588° is obtained in sample S1, which has the best crystalline quality compared to the others and the addition of only 1.7% of In amount results in strong enhancement of dislocation density by ~ 45%. In

addition to HR-XRD measurement, we also performed Raman spectroscopy measurements which is also a powerful technique for studying the InGaAs materials.

3. 2. Raman results:

When clamped onto the substrate, the semiconductor films mainly release the epitaxial stress by forming dislocations [4]. Thus the epitaxial layer morphology is strongly linked to the movement of the dislocations in the epitaxial layer [4].

The strain relaxation can be also investigated by means of Raman scattering in $\text{In}_x\text{Ga}_{1-x}\text{As}$ epitaxial layers as we did here under the (100) back-scattering geometry conditions. As $\text{In}_x\text{Ga}_{1-x}\text{As}$ can be considered in somehow as a mixture of InAs and GaAs parent materials, both InAs-like and GaAs-like phonon modes can be observed according to Raman scattering conditions [22].

Typical Raman spectra of the three $\text{In}_x\text{Ga}_{1-x}\text{As}/\text{InP}$ structures measured at room temperatures with a low excitation intensity in order to avoid laser-induced heating is presented in Figure 2 (a). The laser excitation energy is $E_i=2.33$ eV, which is above the $\text{In}_x\text{Ga}_{1-x}\text{As}$ -layer band gaps. In all samples, the two main phonon bands are related to alloy InGaAs-like and InP-like in the ranges from 190 to 260 cm^{-1} and from 275 to 350 cm^{-1} , respectively [4, 22]. Also, the disorder-activated longitudinal acoustic (DALA) phonon of $\text{In}_x\text{Ga}_{1-x}\text{As}$ samples in the wide Raman band from 100 to 190 cm^{-1} is commonly observed [23, 24]. The reason for this is that there is an interaction between atomic clusters during the development of the epitaxial layer, which results in the disorder degree of crystal arrangement at the interface. The increase in the disorder degree contributes to increase the dislocations density [4].

To quantify the exact peak frequencies of the different active Raman modes, the Raman spectra are deconvoluted using Lorentzian shape function. The error bar in the value of the phonon energy is 0.02 cm^{-1} . The fitting curves for the Raman spectrum of the sample S3 is plotted in Figure 2 (b). At least seven different peaks are necessary to give the best fit to the experimental data. Yet, two peaks are observed for all samples at 299.02 and 333.32 cm^{-1} related to transversal optical (TO) and longitudinal optical (LO) phonon modes of InP substrate, respectively [25]. The spectra also display two-mode Raman peaks around 209.14 and 241.13 cm^{-1} which correspond to LO phonon modes of InAs and GaAs, respectively [4]. Moreover, the peak corresponding to InAs-like LO mode is strong and sharp, due to the rich content of Indium ($x > 0.53$). In this experiment, the InAs-like TO frequency is forbidden in the (100) backscattering geometry. According to the scattering selection rule of zinc-blend

type structure, only LO phonon modes are expected in the (100) backscattering geometry in the **In-rich** $\text{In}_x\text{Ga}_{1-x}\text{As}$ epitaxial layer [26].

By changing the In content, the lattice parameter of $\text{In}_x\text{Ga}_{1-x}\text{As}$ alloy varies between GaAs and InAs ones. As a result, we can observe in the **Figure 2 (a)** a shift of the InAs-Like LO and GaAs-like LO mode towards lower wavenumber with increasing the In content. This shift is due to the compressive strain caused by the lattice mismatch between InP and $\text{In}_x\text{Ga}_{1-x}\text{As}$ [27] and thus is in good agreement with the HR-XRD results.

According to previous studies [4, 28], the relationship between the shift of GaAs-like LO frequency and the residual stress in the $\text{In}_x\text{Ga}_{1-x}\text{As}$ epitaxial layer is given by:

$$\mathcal{R} = \frac{2\omega_0\Delta\omega^{\text{LO}}}{[(S_{11}+2S_{12})(p+2q)-(S_{11}-S_{12})(p-q)]} \quad (3)$$

where

$$\Delta\omega^{\text{LO}} = \omega^{\text{LO}} - \omega_0^{\text{LO}} \quad (4)$$

$$\omega_0^{\text{LO}} = -32x^2 - 18.6x + 290 \quad (5)$$

$$\omega_0 = -0.0003x + 0.16 \quad (6)$$

$$p = 0.268x - 0.427 \quad (7)$$

$$q = 0.126x - 0.478 \quad (8)$$

$$S_{11} = 0.77x + 1.175 \quad (9)$$

$$S_{12} = 0.32x - 0.365 \quad (10)$$

with, x is the In content, p and q are the optical phonon deformation constants, S_{11} and S_{12} are the elastic compliance constants, ω^{LO} is the measured GaAs-like LO frequency in epitaxial layer, ω_0 is optical phonon frequency at $k = 0$, ω_0^{LO} is the frequency of epitaxial $\text{In}_x\text{Ga}_{1-x}\text{As}$ without stress and $\Delta\omega^{\text{LO}}$ is the frequency shift between ω_{LO} and ω_0^{LO} . All parameters and values of equation 3 are summarized in **Table 2**.

For sample S1, S2 and S3, the residual strain in epitaxial layers increases with the increase of indium contents which is consistent with our previous HR-XRD measurements.

3. 3. *Optical study:*

To investigate the influence of indium composition on the optical properties of $\text{In}_x\text{Ga}_{1-x}\text{As}$ ($x = 0.650, 0.665$ and 0.667) thin films grown on (100)InP substrates, photoluminescence (PL) measurements at 10K using a continuous-wave laser with a wavelength of 514 nm were

recorded in all the samples. For the sake of comparison and in order to identify the different energy peaks, PL spectra are normalized and deconvoluted using multiple Gaussian curves (solid lines). **Figure 3** shows normalized PL measurement of all InGaAs samples under an excitation power density of 80 W/cm^2 . Two peaks are observed for all samples. The peak localized between 880-905 nm most likely originates from a band-to-band transition of InP substrate [25]. In addition, a wide PL signal, which belongs to band-band emission of $\text{In}_x\text{Ga}_{1-x}\text{As}$ layer [29], appears at about 1637, 1770 and 1811 nm for samples S1, S2 and S3, respectively. We note that the difference of energy observed between the transitions of InGaAs layer corresponds to the difference in the indium composition (see **Figure 3**). It can be seen that the InGaAs emission shifts from 1637 nm to a higher wavelength of 1811 as the Indium composition increases from 0.65 to 0.667 [30]. Our results demonstrate that these samples are highly suitable for short-wavelength infrared (SWIR, 1.4 – 3 μm) applications. The short-wave infrared (SWIR) band of 1.4–3 μm has attracted increasing attentions for its broad applications, especially in earth observation, night vision and spectral analysis [31]. However, the devices could be optimized for any wavelength within a spectral range of 0.85–3.6 μm .

The FWHM width of the PL signal is within 56–116 meV for all samples. It can be seen that the FWHM of the PL peaks are broadening while the indium content increasing. This effect is due to the mismatch and strain increasing between substrate and the clamped epilayer [25, 30] and can be explained by the presence of the crystal imperfections (surface roughness, dislocations), defects and indium fluctuations in InGaAs epilayer [4, 30]. This high density of structural defects in the InGaAs layer, can generate localized trap states near the band edge, which can be accounted to the asymmetry at the low-energy side in PL peak of InGaAs layer (as indicated by an arrow in **Figure 4**) [17, 31]. Such asymmetry has been attributed to localized excitons which exhibit slightly lower energies due to potential modulations inside the InGaAs layer [17,32]. A similar phenomenon has been already observed in InGaAsP/InAlAs/InP (100) quantum well heterostructure [33].

Here in our films, misfit dislocations could be created by the disorder of cluster arrangement at the interface during the growth process. The results of PL measurements, as well as those obtained by Raman and HR-XRD, are thus in a very satisfactory agreement.

In order to get further insights into the carrier's localization, the power of the excitation line of the InGaAs PL measurements is varied. **Figure 3** shows the PL spectra at 10 K using six different optical excitation power densities (80, 35, 18, 7, 3 and 0.7 W/cm^2). At 0.7 W/cm^2

optical excitation power density, the PL peaks are centered at 0.714, 0.719 and 0.760 eV. By increasing the power density by a factor of ~ 100 to reach a power density of $80\text{W}/\text{cm}^2$, the PL peaks shift toward higher energy by 10 meV. The slight shift of the emission energy observed with increasing excitation power density supports the hypothesis of exciton localization at low temperature. Indeed, for InAlAs/InP, a similar phenomenon was highlighted [17, 18].

Moreover, we have also performed the temperature-dependent photoluminescence (TDPL) measurements from 10 K to 300 K shown in **Figure 5 a, b and c** in sample S1, S2 and S3, respectively. From those PL spectra, we extracted for each temperature the peak position, the integrated intensity and the FWHM as depicted in **Figure 6 a, b and c**, respectively.

Figure 6 (a) shows the PL peak energy positions of InGaAs as a function of temperature. The peak position shows an anomalous behavior (red-blue-red shift) upon increasing temperature from 10K to 300K. The S-shaped form in PL peak emission along the temperature axis can be divided into three temperature intervals and explained as follows:

First the peaks shift to low energies (i.e., red-shift) with increasing temperature, up to approximately 50 K (**region I**). The red-shift is around 8.5 meV, 12.1 meV and 17.2 meV for S1, S2 and S3, respectively. This behavior can be attributed to the recombination of photo-generated carriers trapped by localized states, associated to the tails of the bands. When the temperature is above ~ 60 K, the thermal energy becomes sufficient for the excitons situated in the tails of the bands to reach the strip edges, where they are delocalized to high-energy levels. As a result, a blue shift is observed (**Region II** i.e. $\sim 50\text{K}$ to $\sim 100\text{K}$). For even higher temperatures above ~ 100 K (**Region III**), all carriers are delocalized in the continuum and the shift of the PL peak to lower energies (redshift) prevails, dictated by the thermal dependence of the band gap, which in turn is induced by electron-phonon interaction and lattice thermal expansion [34].

Thus this atypical behavior (S-shaped) of the InGaAs peaks energy can be related to the localized states, due to the inhomogeneous distribution of indium composition [35].

Between samples, there are some differences between S-shape temperature dependence for the localized states of **In-rich** $\text{In}_x\text{Ga}_{1-x}\text{As}$ epitaxial layers emission. The energy separation between the minimum and maximum positions of the S-shaped was defined as the exciton localization energy. This energy is around 5.7 meV, 12.1 meV and 14.5 meV respectively for S1, S2 and S3. It is therefore proposed that there are two kinds of localization states for sample S2 and S3, which are distributed in the InGaAs layers at two distinct energy depths, which is due to the inhomogeneous distribution of indium composition, i.e. with higher

indium composition (deep localization states) and reduced indium composition (shallow localization states), as in sample S1. We explain this difference of the S-shape from one sample to the other by the increasing content of indium in the alloy which increases the lattice-mismatch between InP substrate and epilayer [36]. The lattice-mismatch in epitaxial growth materials significantly degrades the material quality, as shown from the HR-XRD and Raman measurements mentioned above.

In addition to the peak position, the FWHM of the PL peak is another key parameter which likewise provides significant information on the localization mechanism of carriers. The FWHM behavior against temperature of each samples under high excitation power density P_0 is plotted in **Figure 6 (b)**. The line width versus temperature exhibits non-monotonic behavior, which brings further insights to the carriers' localization mechanism. Indeed, the PL linewidth continuously increases till a temperature of ≈ 200 K and then slowly drops down above this temperature for the all samples. The widening of the PL signal with temperature can be explained by the transfer and the thermalization from localized states. Indeed, when the temperature rises up to the thermalization point, some of localized carriers occupy shallow localized states [32]. This consequently leads to an increase of the FWHM. Here, when approaching 200 K, most localized carriers become progressively mobile [37]. Note that this temperature behavior is more pronounced in case of sample S3 which is the more defective one.

Finally, the temperature dependence of the normalized PL intensity is reported in **Figure 6 (c)**. By increasing the temperature, the global emission intensity of the PL spectra gradually diminishes, showing the existence of non-radiative recombination centers.

In order to understand the mechanism of carrier thermal quenching in InGaAs layer, we fit the experimental data of the integrated PL intensity by using the following Arrhenius-like expression [37, 38]:

$$I(T) = \frac{I_0}{1 + \sum_i c_i \exp\left(\frac{E_{ai}}{k_B T}\right)} \quad (10)$$

Where T is the measured temperature, $I(T)$ is the integrated PL emission intensity, I_0 is a variable parameter, k is Boltzmann's constant, c_i are constants related to the densities of non-radiative recombination centers, E_{ai} are the activation energies corresponding to the non-radiative recombination centers.

Figure 7 shows the fit using equation (10) of the experimental data, and the activation energies obtained from the fit for each sample are also indicated. Those activation energies

are 15, 22 and 27 meV for the samples S1, S2 and S3. It is worth pointing out that when the indium composition increases, the thermal activation energy increases. This could be understood as a consequence of the strongest trapping effect by the defects in case of sample S3 which requires a stronger activation energy to release the charge carriers from their localized states.

4. Conclusion

To sum up, the structural and optical properties of **In-rich** $\text{In}_x\text{Ga}_{1-x}\text{As}$ epitaxial layers grown on (100) InP structures have been investigated by HR-XRD, Raman and PL spectroscopies.

The effect of different indium contents on the crystalline quality and optical properties was investigated. We have successfully grown epitaxial $\text{In}_x\text{Ga}_{1-x}\text{As}$ films with relatively **rich** indium content of $x=0.667$ without using any buffer layer. We have clearly showed that by increasing the lattice mismatch with the increase of indium content, the crystal structure releases the epitaxial stress by created defects which are likely dislocations for whom we estimated the density. This structural defect are proposed as the carrier's localization centers as supported by our PL measurements. For instance, TDPL results reveal that the inverted S-shape along temperature axis results from transition process between localized and delocalized states in the InGaAs layer, which depends on indium amount and its relatively inhomogeneous distribution.

Our work provides new insights into the understanding of the photoluminescence response in $\text{In}_x\text{Ga}_{1-x}\text{As}$ with **rich** In composition.

Reference:

- [1] T. Asar, S. Özçelik, E. Özbay, Structural and Electrical Characterizations of $\text{In}_x\text{Ga}_{1-x}\text{As}/\text{InP}$ Structures for Infrared Photodetector Applications, *J Appl Phys.* 115 (2014) 104502.
- [2] I. Demir, I. Altuntas, B. Bulut, M. Ezzedini, Y. Ergun, and S. Elagoz, Comprehensive Growth and Characterization Study on Highly n-doped InGaAs as a Contact Layer for Quantum Cascade Laser Applications, *Semicond. Sci. Technol.* 33 (2018) 055005.
- [3] S. Adhikary, S. Chakrabarti, Spectral Broadening Due to Post-Growth Annealing of a Long-Wave InGaAs/GaAs Quantum Dot Infrared Photodetector with a Quaternary Barrier Layer, *Thin Solid Films* 552 (2014) 146-149.
- [4] L. Zhao, Z. Guo, M. Zhang, S. Yang, L. Zhao, Surface-Interface Analysis of $\text{In}_x\text{Ga}_{1-x}\text{As}/\text{InP}$ Heterostructure in Positive and Negative Mismatch System, *Surf. Interface Anal.* 51 (2019) 498–505.
- [5] I. Demir, S. Elagoz, Interruption Time Effects on InGaAs/InAlAs Superlattices of Quantum Cascade Laser Structures Grown by MOCVD, *Superlattice. Microst.* 100 (2016) 723-729.
- [6] R. W. Hoogeveen, A. P. Goede, Extended wavelength InGaAs infrared (1.0–2.4 μm) detector arrays on SCIAMACHY for space-based spectrometry of the Earth atmosphere, *Infrared Phys. Technol.* 42 (2001) 1-16.
- [7] R.E. Nahory, M.A. Pollack, W.D. Johnson Jr, R.L. Barns, Band Gap Versus Composition and Demonstration of Vegard Law for $\text{In}_{1-x}\text{Ga}_x\text{As}_y\text{Py}$ Lattice Matched to InP, *Appl. Phys. Lett.* 33 (1978): 659-661.
- [8] Y. Uliel, D. Cohen-Elias, N. Sicon, I. Grimberg, N. Snapi, Y. Paltiel, M. Katz, InGaAs/GaAsSb Type-II Superlattice Based Photodiodes for Short Wave Infrared Detection, *Infrared Physics & Technology*, 84, (2017), 63-71.
- [9] Q. L. Kleipool, R. T. Jongma, A. M. S. Gloudemans, H. Schrijver, G. F. Lichtenberg, R. M. van Hees, A. N. Maurellis, R. W. M. Hoogeveen, In-flight Proton-induced Radiation

Damage to SCIAMACHY's Extended-Wavelength InGaAs Near-Infrared Detectors, *Infrared Phys. Technol.* 50 (2007) 30-37.

[10] A. Rogalski, P. Martyniuk, InAs/GaInSb Superlattices as a Promising Material System for Third Generation Infrared Detectors, *Infrared Phys. Technol.* 48 (2006) 39–52.

[11] B. Du, Y. Gu, X.Y. Chen, Y. J. Ma, Y. H. Shi, J. Zhang, and Y. G. Zhang, Improved Performance of High Indium InGaAs Photodetectors with InAlAs Barrier, *JPN. J. Appl. Phys.* 57 (2018) 060302.

[12] T. Sasaki, H. Suzuki, A. Sai, M. Takahasi, S. Fujikawa, I. Kamiya, Y. Ohshita, M. Yamaguchi, Growth Temperature Dependence of Strain Relaxation During InGaAs/GaAs(001) Heteroepitaxy. *J Cryst Growth.* 323 (2011) 13-16.

[13] X. Y. Chen, Y. Gu and Y. G. Zhang, Epitaxy and Device Properties of InGaAs Photodetectors with Relatively High Lattice Mismatch. (2017) In: *Epitaxy*. IntechOpen <http://dx.doi.org/10.5772/intechopen.70259>.

[14] X. Ji, B. Liu, H. Tang, X. Yang, X. Li, H. Gong, B. Shen, P. Han, F. Yan, 2.6 μm MBE Grown InGaAs Detectors with Dark Current of SRH and TAT. *AIP Advances*, 4 (2014), 087135.

[15] Y.Mao, X.X.Liang, G.J.Zhao, T.L.Song, The structural and optical properties of ternary mixed crystals $\text{In}_x\text{Ga}_{1-x}\text{As}$ with zinc-blende structure by first-principle calculations, *Physica B: Condensed Matter*, 569 (2019) 87-95.

[16] X. Ji, X. Chen, X. Yang, X. Zhang, J. Shao, T. Yang, Self-Seeded MOCVD Growth and Dramatically Enhanced Photoluminescence of InGaAs/InP Core–Shell Nanowires, *Nanoscale Research Letters* 13 (2018) 269.

[17] B. Smiri, T. Hidouri, F. Saidi, H. Maaref, Carriers' Localization and Thermal Redistribution in InAlAs/InP Grown by MOCVD on (311)A- and (311)B-InP Substrates, *Appl. Phys. A-Mater* 125 (2019) 134.

[18] B. Smiri, I. Fraj, F. Saidi, R. Mghaieth, H. Maaref, Effect of Piezoelectric Field on Type II Transition in InAlAs/InP (311) Alloys with Different Substrate Polarity, *J. Alloy. Compd.* 736 (2018) 29-34.

- [19] F. Martelli, A. Polineni, A. Patane, M. Capizzi, P. Borri, M. Gurioli, M. Colocci, A. Bosacchi, S. Franchi, Exciton Localization by Potential Fluctuations at the interface of InGaAs/GaAs Quantum Wells, *Phys. Rev. B.* 53 (1996) 11.
- [20] V. Swaminathan, A. T. Macrander, *Materials Aspects of GaAs and InP Based Structures.* New Jersey: Prentice-Hall, Inc. 91 (1991).
- [21] S. Z. Chang, T. C. Chang, J. L. Shen, S. C. Lee, Y. F. Chen, Material and Electrical Properties of Highly Mismatched $\text{In}_x\text{Ga}_{1-x}\text{As}$ on GaAs by Molecular-beam Epitaxy, *J. Appl. Phys.* 74 (1993) 6912.
- [22] M. Zhang, Z. Guo, L. Zhao, S. Yang and L. Zhao, The Effect of Buffer Types on the $\text{In}_{0.82}\text{Ga}_{0.18}\text{As}$ Epitaxial Layer Grown on an InP (100) Substrate, *Materials* 11 (2018) 975.
- [23] M. S. Park, M. Razaeei, K. Barnhart, C. L. Tan, H. Mohseni, Surface Passivation and Aging of InGaAs/InP Heterojunction Phototransistors, *J. Apply. Phys.* 121 (2017) 233105.
- [24] H. Kawamura, R. Tsu, L. Esaki, Disorder-Activated Acoustic Mode in Raman Spectrum of $\text{Ga}_x\text{Al}_{1-x}\text{As}$, *Phys. Rev. Lett.* 29 (1972) 1397.
- [25] B. Smiri, F. Saidi, A. Mlayah, H. Maaref, Effect of Substrate Polarity on the Optical and Vibrational properties of (311)A and (311) B Oriented InAlAs/InP Heterostructures, *Physica E.* 112 (2019) 121-127.
- [26] L. Pavesi, R. Houdre, P. Giannozzi, Strain and Alloying Effects on the Electronic and Vibrational Properties of $\text{In}_y\text{Al}_{1-y}\text{As}$ on InP, *J. Appl. Phys.* 78 (1995) 470.
- [27] A. Sayari, N. Yahyaoui, M. Oueslati, H. Maaref, K. Zellama, Raman Study of V/III Flux Ratio Effect in InP/InAlAs/InP Heterostructures Grown by MOCVD, *J. Raman Spectrosc.* 40 (2009) 1023–1027.
- [28] Jinping Li, Guoqing Miao, Zhiwei Zhang and Yugang Zeng, Experiments and Analysis of the Two-Step Growth of InGaAs on GaAs Substrate, *Cryst Eng Comm.* 17 (2015) 5808-5813.
- [29] T. Lin, H. Sun, H. Zhang, Y. Wang, N. Lin, X. Ma, Research on the High Indium Content InGaAs Multiple Quantum Wells Wafers for $k > 1.55 \mu\text{m}$ Laser Diodes, *J. Alloy. Compd.* 631 (2015) 283–287.

- [30] W. Q. Chen, S. K. Hark, Strain Induced Effects in (111) Oriented InAsP/InP, InGaAs/InP, and InGaAs/InAlAs Quantum Wells on InP Substrates, *J. Appl. Phys.* 77 (1995) 5747-5750.
- [31] Y. G. Zhang, Y. Gu, Gas Source MBE Grown Wavelength Extending InGaAs Photodetectors. In: Betta GFD, editor. *Advances in Photodiodes*. Croatia: InTouch; (2011) 349-376.
- [32] B. Smiri, I. Fraj, M. Bouzidi, F. Saidi, A. Rebey, H. Maaref, Effect of V/III ratio on the optical properties of (311)A and (311) B oriented InAlAs/InP heterostructures. *Results Phys.* 12 (2019) 2175 –2182.
- [33] F. Peiró, J. C. Ferrer, A. Cornet, M. Calamitrou, A. Georgakilas, Lateral Modulations in InAlAs/InP and InGaAs/InP Systems, *phys. stat. sol. (a)* 195 (2003) 32–37.
- [34] H. Esmailpour, V. R. Whiteside, L. C. Hirst, J. G. Tischler, R.J. Walters, Ian R. Sellers, The Effect of an InP Cap Layer on the Photoluminescence of an $\text{In}_x\text{Ga}_{1-x}\text{As}_{1-y}\text{P}_y/\text{In}_z\text{Al}_{1-z}\text{As}$ Quantum Well Heterostructure, *J. Appl. Phys.* 121 (2017) 235301.
- [35] H. N. Wang, Z. W. Ji, S. Qu, G. Wang, Y. Z. Jiang, B. L. Liu, X. G. Xu, H. F. Mino Influence of Excitation Power and Temperature on Photoluminescence in InGaN/GaN Multiple Quantum Wells. *Opt. Express.* 20 (2012) 3392–3940.
- [36] B. Smiri, F. Saidi, A. Mlayah, H. Maaref. Power- and temperature-dependent photoluminescence investigation of carrier localization at inverted interface transitions in InAlAs/InP structures. *Jpn. J. Appl. Phys.* 59, (2020), 022001.
- [37] X. Ji, X. Chen, X. Yang, X. Zhang, J. Shao, T. Yang, Self-Seeded MOCVD Growth and Dramatically Enhanced Photoluminescence of InGaAs/InP Core–Shell Nanowires, *Nanoscale Res. Lett.* 13 (2018) 269.
- [38] X. Wang, F. Liang, D. Zhao, D. Jiang, Z. Liu, J. Zhu, J. Yang, W. Wang, Effect of Dual-Temperature-Grown InGaN/GaN Multiple Quantum Wells on Luminescence Characteristics, *J. Alloy. Compd.* 790 (2019) 197-202.
- [39] Y. Gu, Y.G. Zhang, A. Z. Li, K. Wang, C. Li, Y. Y. Li, Structural and Photoluminescence Properties for Highly Strain-Compensated InGaAs/InAlAs Superlattice. *Chin. Phys. Lett.* 26 (2009) 077808.

Tables captions

Sample	Indium Contents (%)	Lattice (Å)	FWHM (degree)	Dislocation density (10^9 cm^{-2})
S1	65	5.9545	0.588	2.17
S2	66.1	5.9592	0.650	2.64
S3	66.7	5.9618	0.709	3.14

Table 1: The HR-XRD results of the InGaAs epitaxial layers with different In.

Sample	Indium Contents (%)	ω_0^{LO} (cm^{-1})	ω^{LO} (cm^{-1})	$\Delta\omega^{\text{LO}}$ (cm^{-1})	ω_0 (10^{14} S^{-2})	\mathcal{R} (GPa)
S1	65	264.39	249.21	-15.18	0.1598	2.88
S2	66.1	263.72	243.52	-20.20	0.1598	3.80
S3	66.7	263.36	241.13	-22.59	0.1598	4.17

Table 2: The Raman results of the $\text{In}_x\text{Ga}_{1-x}\text{As}$ epitaxial layers with different In.

Figures captions

Figure 1: $2\theta/w$ X-Ray diffraction spectra of the InGaAs layers having different In alloys grown on InP by MOVPE.

Figure 2: (a) Raman spectra recorded at room temperature with incident energy $E_i = 2.33$ eV for the all samples. (b) Line shape fitting of Raman spectrum obtained from sample S3.

Figure 3: 10K PL spectra obtained from samples S1, S2 and S3 at different type of Indium concentration (excitation laser power was 80 W/cm² for all the samples).

Figure 4: PL spectra of samples S1 (a), S2 (b) and S3 (c) at several different excitation powers, measured under temperatures of 10K.

Figure 5: PL spectra of sample S1 (a), S2 (b) and S3 (c) at a temperature range of 10–300 K, measured under excitation powers of 80 W/cm².

Figure 6: (a) PL peak energy shift, (b) The PL FWHM and (c) integrated PL intensity vary as a function of temperature for all samples measured at the laser excitation intensity of $I_0 = 80$ W/cm².

Figure 7: Temperature-dependent integrated PL intensity of samples S1, S2 and S3 at the excitation power of 80 W/cm².

Figure 1 :

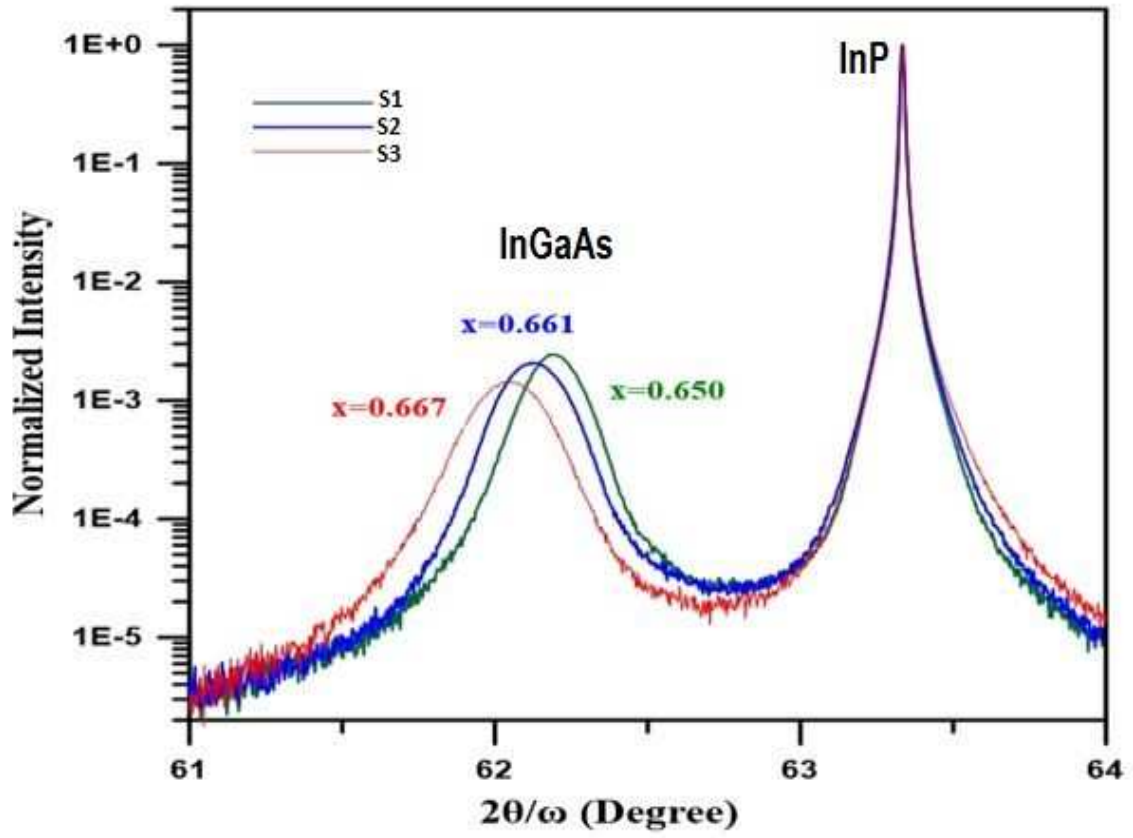
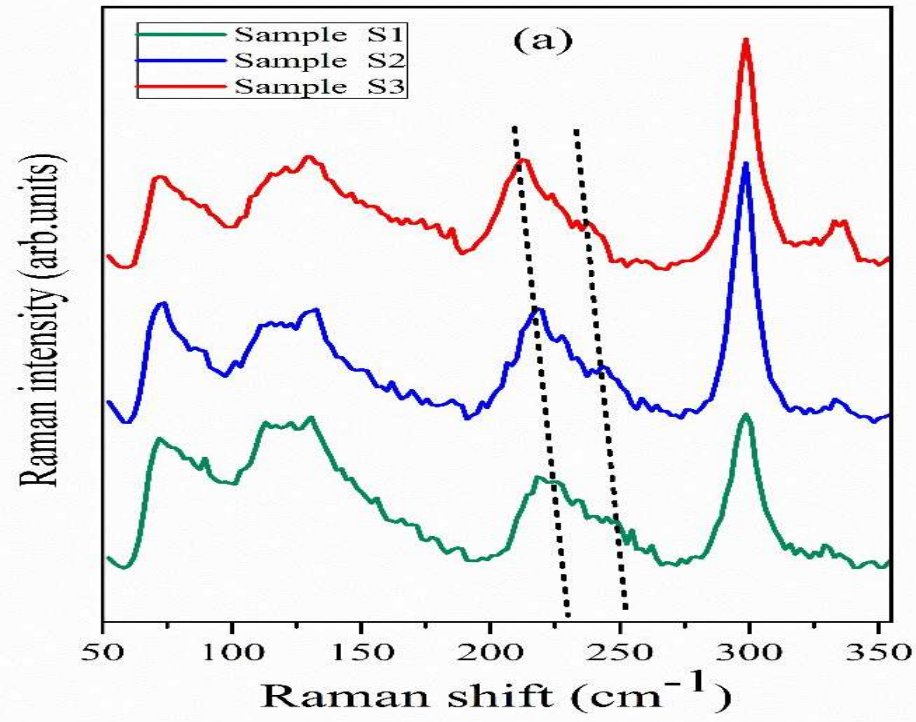


Figure 2:



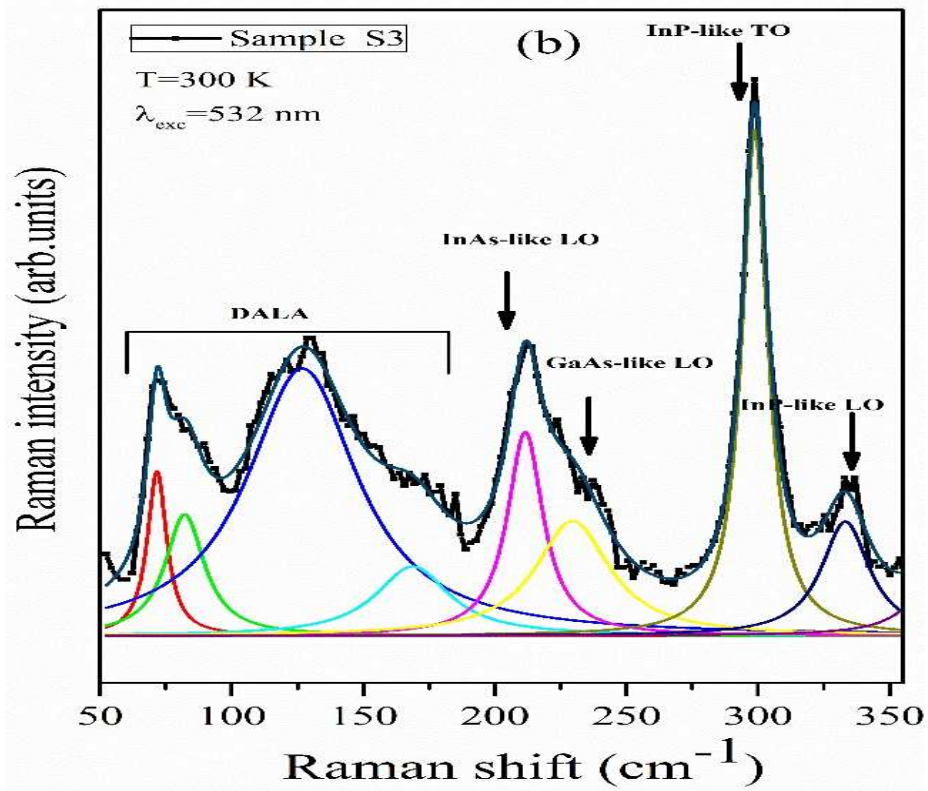


Figure 3:

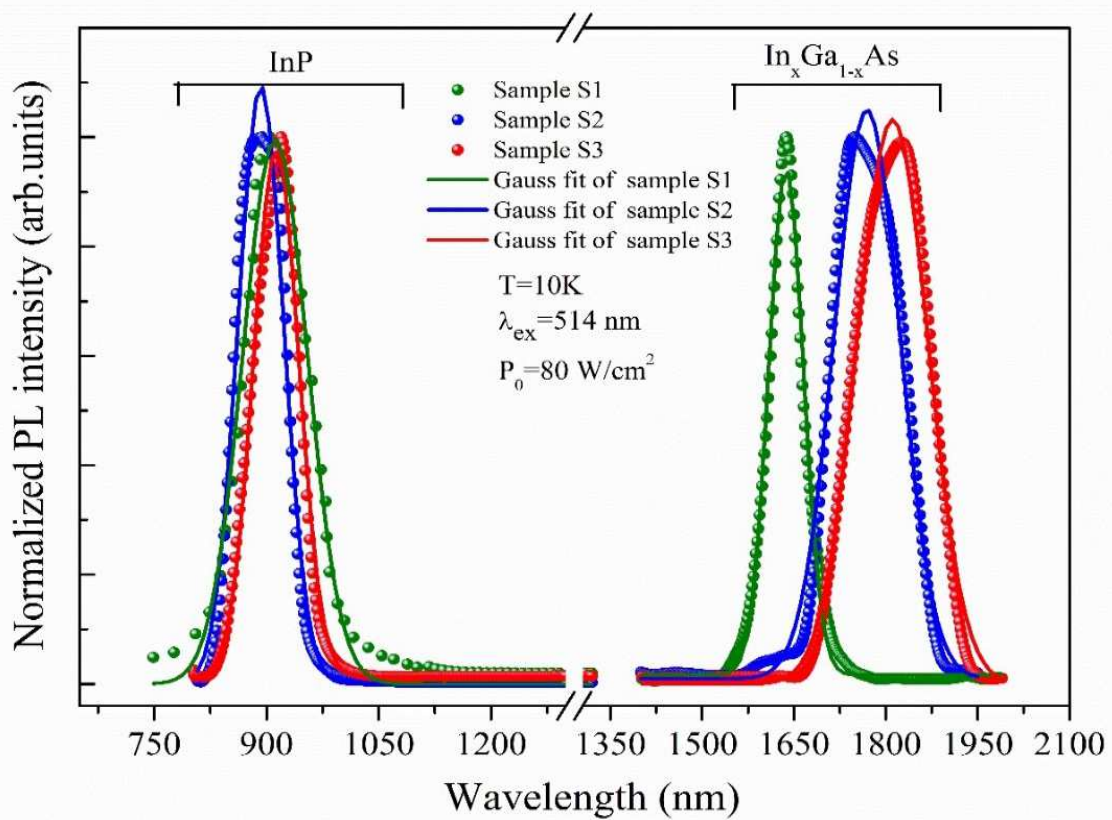


Figure 4:

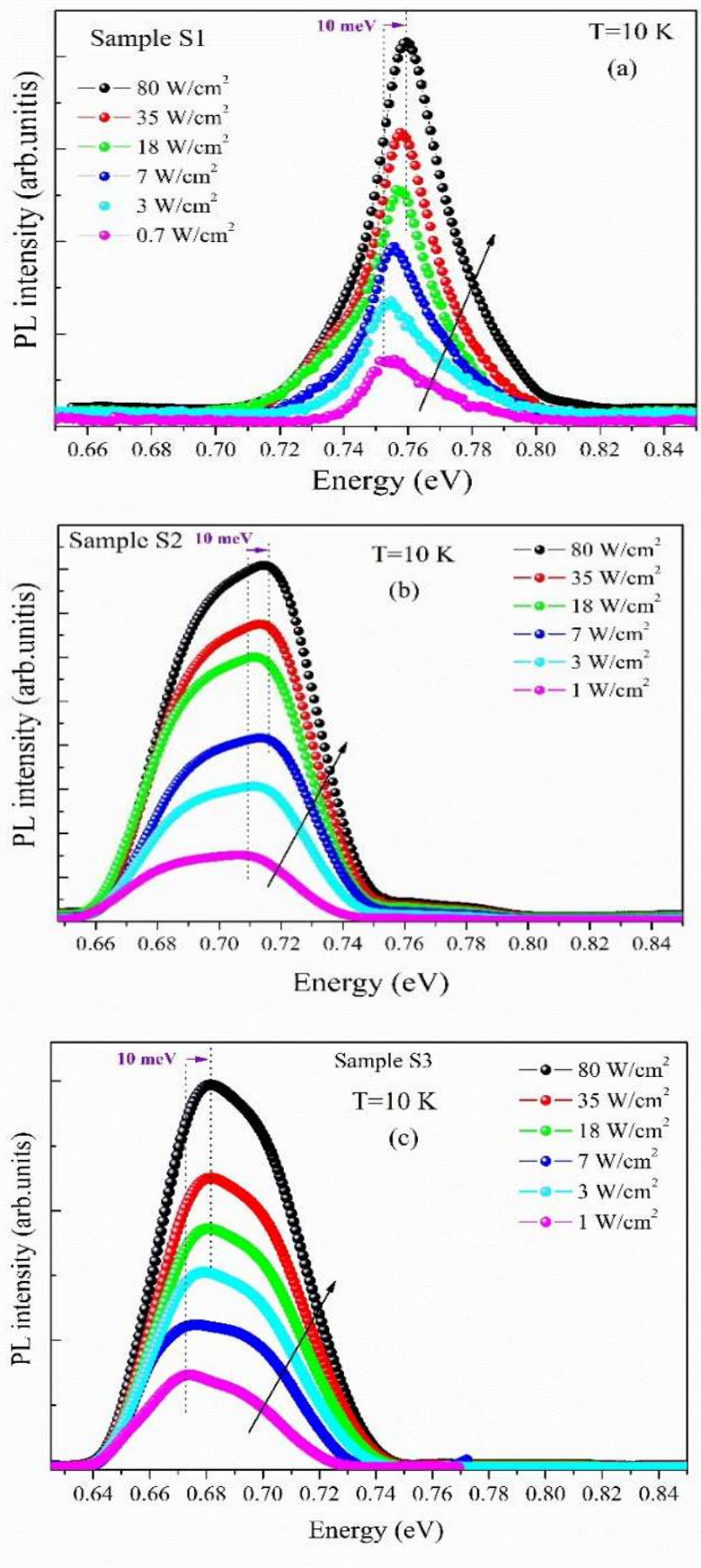


Figure 5:

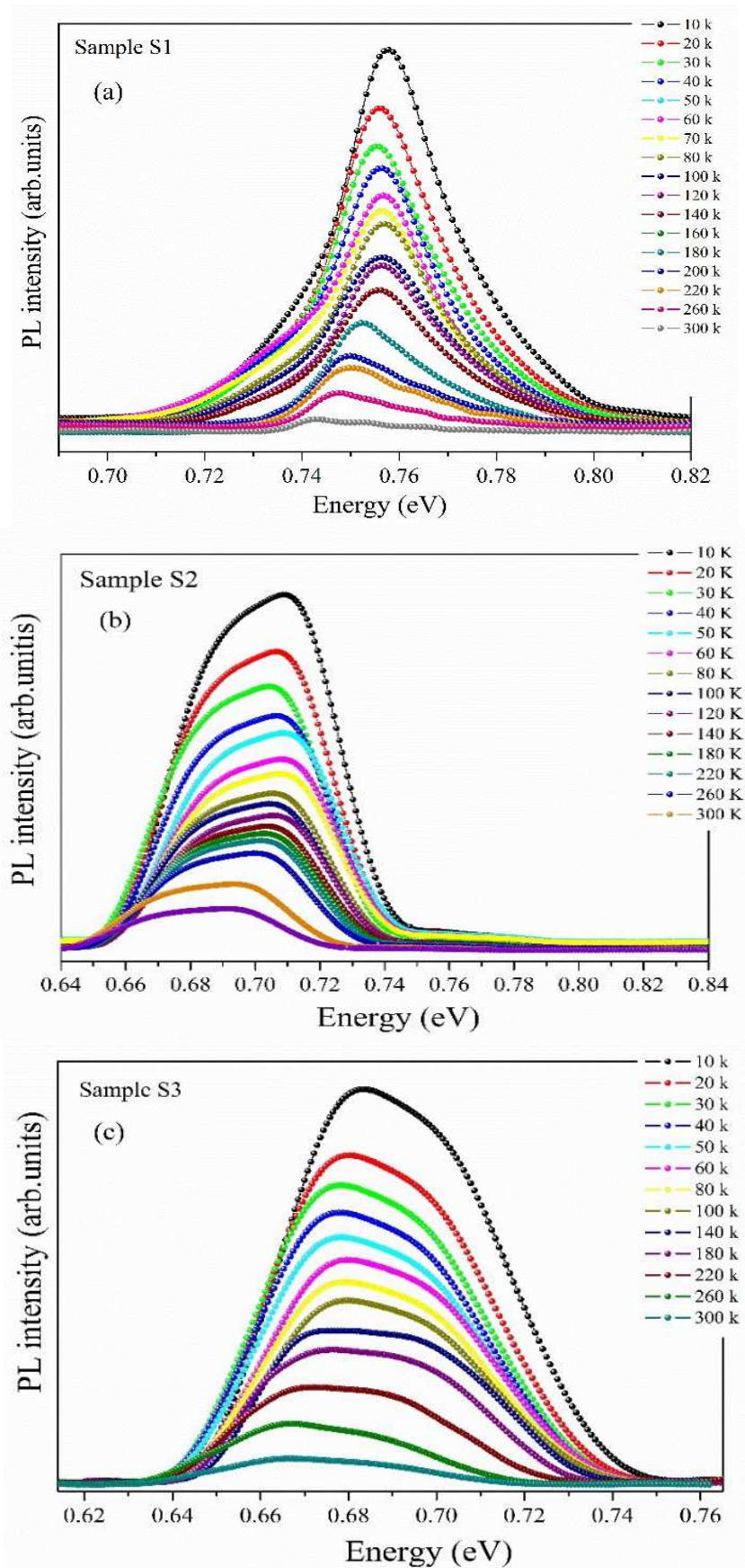


Figure 6:

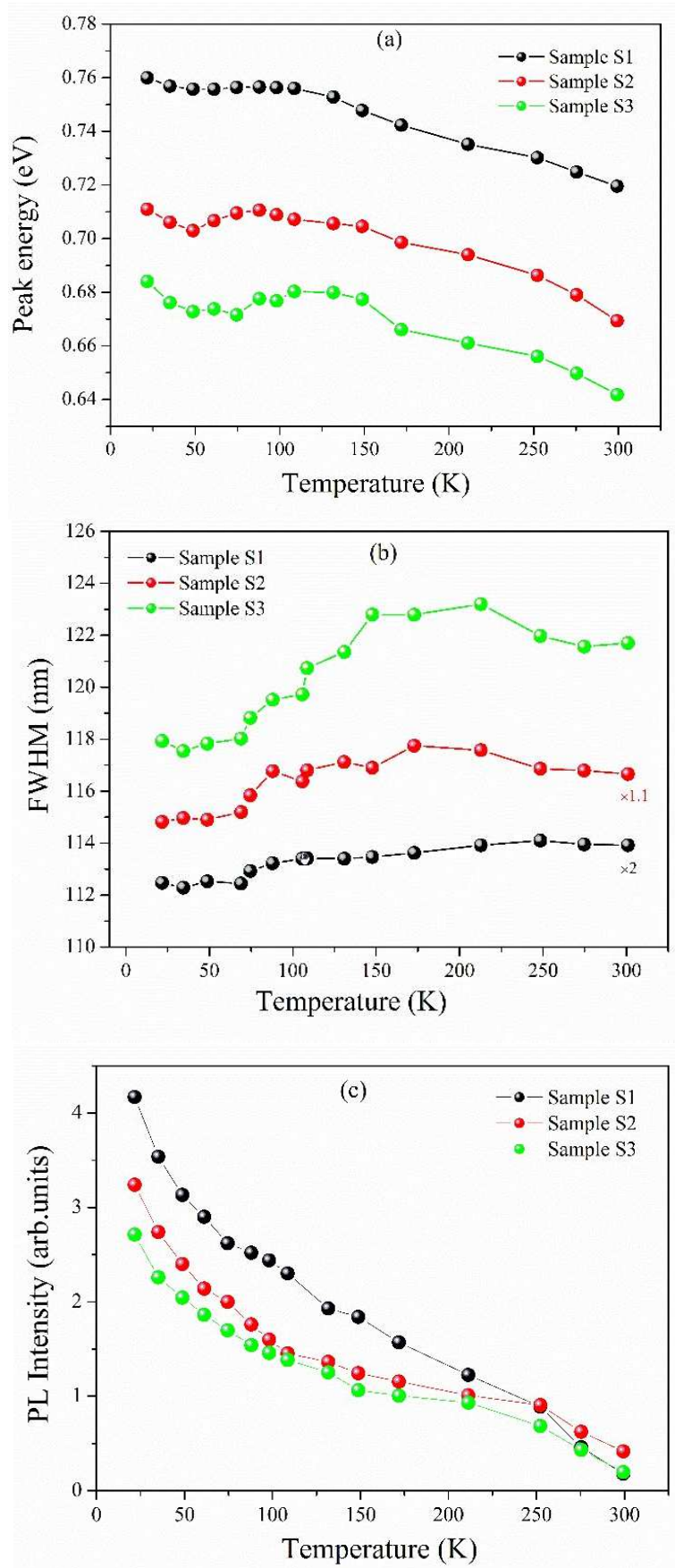


Figure6:

